

Probing Thermomechanics at the Nanoscale: Impulsively Excited Pseudosurface Acoustic Waves in Hypersonic Phononic Crystals

Damiano Nardi,^{*,†,‡} Marco Travaglini,^{‡,§} Mark E. Siemens,^{||} Qing Li,[†] Margaret M. Murnane,[†] Henry C. Kapteyn,[†] Gabriele Ferrini,[‡] Fulvio Parmigiani,[⊥] and Francesco Banfi[‡]

[†]JILA, University of Colorado at Boulder, Boulder, Colorado 80309, United States

[‡]Dipartimento di Matematica e Fisica, Università Cattolica del Sacro Cuore, I-25121 Brescia, Italy

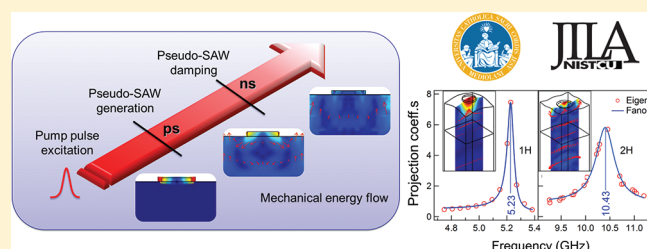
[§]Center for Nanotechnology Innovation @NEST, Istituto Italiano di Tecnologia, I-56127 Pisa, Italy

^{||}Department of Physics and Astronomy, University of Denver, Denver, Colorado 80208, United States

[⊥]Dipartimento di Fisica, Università degli Studi di Trieste and Sincrotrone Trieste, I-34012 Basovizza, Trieste, Italy

ABSTRACT: High-frequency surface acoustic waves can be generated by ultrafast laser excitation of nanoscale patterned surfaces. Here we study this phenomenon in the hypersonic frequency limit. By modeling the thermomechanics from first-principles, we calculate the system's initial heat-driven impulsive response and follow its time evolution. A scheme is introduced to quantitatively access frequencies and lifetimes of the composite system's excited eigenmodes. A spectral decomposition of the calculated response on the eigemodes of the system reveals asymmetric resonances that result from the coupling between surface and bulk acoustic modes. This finding allows evaluation of impulsively excited pseudosurface acoustic wave frequencies and lifetimes and expands our understanding of the scattering of surface waves in mesoscale metamaterials. The model is successfully benchmarked against time-resolved optical diffraction measurements performed on one-dimensional and two-dimensional surface phononic crystals, probed using light at extreme ultraviolet and near-infrared wavelengths.

KEYWORDS: Metamaterials, nanomechanics, ultrafast optics, surface acoustic waves, phononic crystals, Fano resonance



Surface acoustic waves (SAWs) are surface-confined elastic oscillations that take place in a semi-infinite solid and are of great interest because of their high sensitivity to the mechanical properties of the material in which they propagate. Their penetration depth corresponds to a fraction of the wavelength of excitation, making SAWs an appealing tool for studying the properties of thin films, including interface properties and the mechanical response of nanostructures deposited on, or embedded within, the surface.^{1,2} Studying nanostructured samples of ever decreasing size requires generating and detecting highly surface-confined SAWs with correspondingly short wavelengths. A surface phononic crystal (SPC, a periodic array of nanostructures patterned on an optically transparent or semitransparent substrate) can be impulsively excited with an ultrashort laser pulse, launching a pseudosurface acoustic wave (pseudo-SAW) with wavelength limited only by the resolution of the pattern fabrication technique.^{3–5} Upon nanopatterning the surface of a substrate to obtain a SPC, the SAW typical of a semi-infinite solid evolves into a pseudo-SAW, an acoustic wave partially localized on the nanostructures and radiating mechanical energy into the substrate due to the scattering introduced by the periodic overlayer.⁶

Accurate modeling of the frequency and lifetime of the resulting optically excited pseudo-SAWs without using free parameters is critical in view of applications. For example, nondestructive

photoacoustic “high frequency sonar” testing of nanoelectronics,⁷ modulation of photonic structures for photovoltaic applications, high-resolution acoustic imaging of nanodevices or living cells for nanomedicine purposes,⁸ and application of pseudo-SAW modes for future SPC mass sensor devices operating in the hypersonic range⁹ will all rely on the knowledge of the acoustic wave propagation and dissipation in complex nanostructures. This Letter presents the first complete ab initio analysis of the dynamics involved in the ultrafast optical excitation of pseudo-SAWs in hypersonic SPCs. The proposed scheme allows access to the excited pseudo-SAWs frequency and lifetime, and theoretical predictions are positively benchmarked against time-resolved optical diffraction measurements.

Numerous studies have described the mechanical properties and optical excitation of surface acoustic waves on SPCs.^{3,10,11} These studies have made it clear that when a SPC is excited by a short-pulse laser, the observed perturbation is predominantly a collective excitation across the structure, as opposed to exciting the eigenmodes of the individual nanostructures.^{5,12,13} The character of these surface oscillations has been recently formally addressed in the static case in terms of pseudo-SAW solutions.^{6,14}

Received: June 1, 2011

Revised: September 2, 2011

Published: September 12, 2011

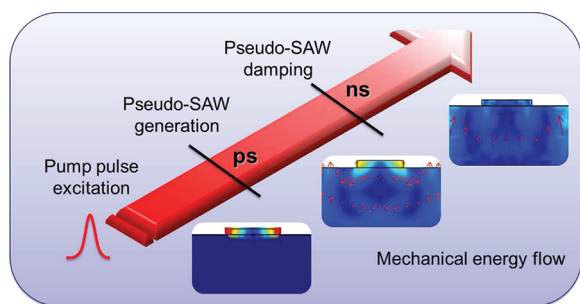


Figure 1. Time-line of the thermomechanics triggered by ultrafast laser pulses in SPCs. Upon absorption of the laser pump pulse the nanostructures' electrons and phonons thermalize, reaching mutual temperature equilibrium on the subpicosecond to picosecond time scale. Subsequently, on the few picosecond time scale, the nanostructures' thermal expansion launches pseudo-SAWs in the SPC. Both thermal and mechanical relaxation to the substrate take place on the nanosecond time scale.

However an exhaustive ab initio analysis of the dynamics following ultrafast optical excitation of hypersonic SPCs is still lacking, as is any scheme allowing access to the excited eigenmodes' frequencies and lifetimes.

In this paper, the thermomechanics of impulsive SPC excitation is modeled from first-principles, calculating both the initial heat-driven displacement and its time evolution. Spectral analysis of the dynamics reveals the surface phononic crystal's eigenmodes, which are shown to exhibit Fano-type resonance spectral profiles that result from the coupling between surface and bulk acoustic modes. This model makes it possible to resolve which eigenmodes are impulsively excited (primarily pseudo-SAWs) and their lifetimes. Our continuum model also provides a solid base for the simple fit models used previously to interpret time-resolved reflectivity measurements. To test our model, we perform time-resolved optical diffraction measurements in both one-dimensional (1D) and two-dimensional (2D) surface phononic crystals, using very different material combinations and probing wavelengths.

Time Scales of Thermomechanics. Our experiment and theory are first performed in a 1D-SPC geometry, consisting of periodic nickel stripes deposited on a sapphire substrate. As shown in Figure 1, the basic idea behind a time-resolved diffraction (TRD) experiment is the following: an intense laser pump pulse, focused on an area A of the surface, impulsively delivers an energy δU within the light penetration depth Λ , the energy density being peaked within the metallic nanostructures. Starting from this instant, the physics is best pictured by a three-step sequence.¹⁵ In the first step, the ultrashort laser pulse heats the electron gas in the metallic nanostructures (subpicosecond time scale). In the second step, the hot electron gas thermalizes with the nanostructures' lattice (picosecond time scale). In the third step, the local temperature increase δT is responsible for a sudden lattice expansion through the thermal expansion coefficient α . At this point, (a) the impulsive expansion of the periodic nanostructures, mechanically coupled to the substrate, causes a spatially modulated stress on the surface of the substrate, and launches a pseudo-SAW of wavelength λ matching the phononic crystal's periodicity; (b) the nanostructures thermalize with the substrate (subnanosecond and nanosecond time scale). This three-step sequence repeats itself upon arrival of a new laser pulse each $1/f_{\text{rep}}$ seconds, where f_{rep} is the laser repetition rate.

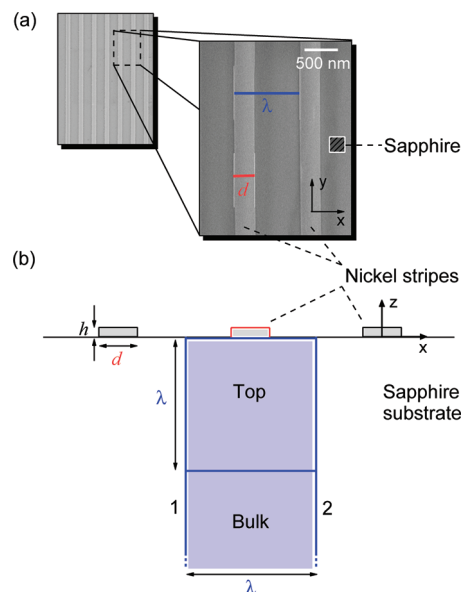


Figure 2. SEM image and schematic diagram of a 1D surface phononic crystal. (a) Isotropic nickel stripes of width $d = 250$ nm and height $h = 20$ nm are deposited on a sapphire substrate. The grating has period $\lambda = 1058$ nm. (b) The top $2 \mu\text{m}$ portion of the 1D simulation unit cell is reported. The cell geometry is divided in three parts for a straightforward evaluation of the SAW-likeness coefficient: Ni stripe, sapphire substrate's top region of depth λ , and sapphire bulk.

The dynamics of the phononic crystal are followed by monitoring the relative diffracted intensity variation of a delayed laser probe pulse as measured on the first order of diffraction, $\Delta I_{1d}/I_{1d}$. The signal is modulated by the nanostructures' form factor variation in time.^{4,13,16}

We consider an SPC in which the nickel stripes have width $d = 250$ nm and height $h = 20$ nm, whereas the grating period is $\lambda = 1058$ nm, thus giving a filling fraction $f = d/\lambda \sim 0.24$, as pictured in Figure 2. The laser source adopted to investigate the 1D-SPC is an ultrafast Ti/sapphire oscillator-amplifier system generating 25 fs pulses at $f_{\text{rep}} = 2$ kHz, 2 mJ per pulse, 800 nm central wavelength, pump beam spatial extension at full width at half-maximum (fwhm) $d_{\text{pump}} = 700 \mu\text{m}$. The pump pulse is at 800 nm wavelength, whereas the probe beam is in the extreme ultraviolet (EUV), obtained by high harmonic generation (HHG) in an Ar gas-filled waveguide driven by a portion of the original 800 nm pulse. Further details can be found in Siemens et al.^{5,17}

Heat-Driven Impulsive Displacement. The thermal dynamics is accounted for starting from the laser parameters, the Ni and Al_2O_3 optical constants,¹⁸ the electronic and lattice specific heats,¹⁹ the electron–phonon coupling in the nanostructure, and the thermal boundary resistivity between the two materials.^{13,17} The physics entailed in the first two time steps is formalized in terms of the two-temperature model and a Kapitza-like boundary condition. At this stage, the temperature of the sapphire substrate T_{sapph} remains substantially unaltered. The time evolution of the electron T_{el} and phonon T_{ph} temperatures of the metallic stripes is thus calculated. The maximum lattice temperature in the nanostructures is reached at a time delay $t_0 = 4$ ps at which time the electron gas has effectively thermalized with the lattice. From this instant, the thermodynamical temperature of the nanostructures is defined, and it is higher than T_{sapph} .¹⁵ The impulsive temperature mismatch $\delta T = T_{\text{ph}} - T_{\text{sapph}} \sim 60$ K

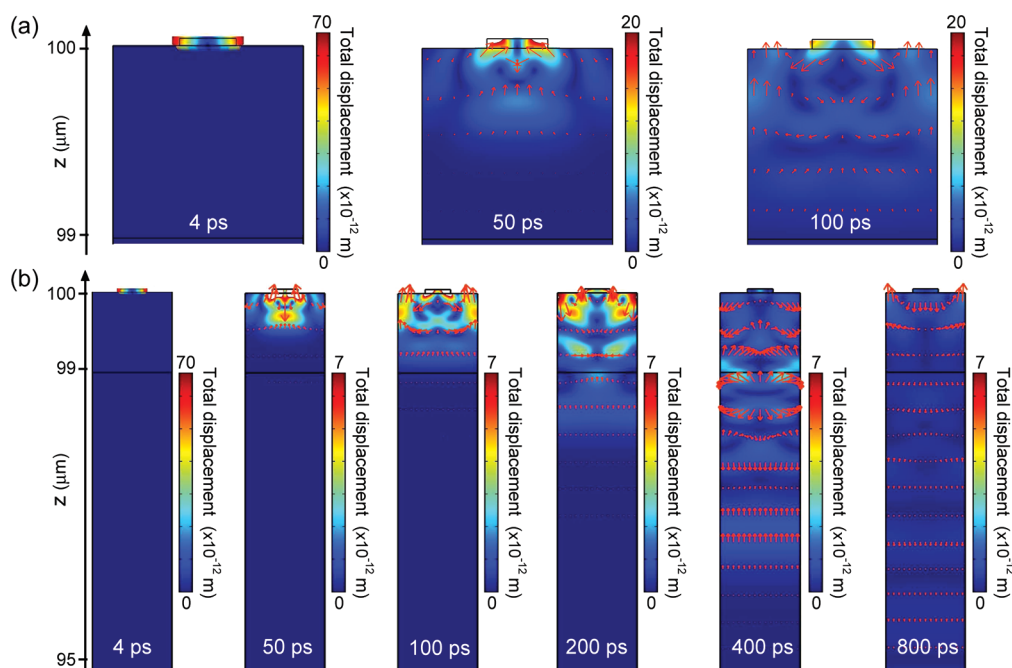


Figure 3. (a) Pseudo-SAW generation sequence and short-range temporal evolution. The profile deformation and arrows in the simulation unit cell correspond to the displacement field. The color scales refer to the absolute total displacement. (b) Landscape view of the pseudo-SAW generation and long-range temporal evolution.

triggers a nonequilibrium expansion of the nanostripes. The expansion is governed by $\delta x/x = \alpha^* \delta T \sim 5 \times 10^{-4}$, where x refers to both the nanostructure's width d and height h , and α^* is the effective thermal expansion coefficient of the Ni-sapphire system.¹³ The corresponding total displacement profile $\mathbf{u}(\mathbf{r}, t_0)$ of the expanded nanostripe at t_0 is shown in Figure 3. The displacement $\mathbf{u}(\mathbf{r}, t_0)$ and velocity $\dot{\mathbf{u}}(\mathbf{r}, t_0)$ fields are taken as the initial condition for the dynamics. The initial velocity field is $\dot{\mathbf{u}}(\mathbf{r}, t_0) = 0$. In fact, the kinetic energy is null when the potential energy is maximum, which occurs at t_0 when the lattice thermal expansion is at a maximum. The acoustic dynamics is ruled by the equation of motion for the composite system

$$\nabla \cdot [\mathbf{c}(\mathbf{r}) : \nabla \mathbf{u}] = \rho(\mathbf{r}) \ddot{\mathbf{u}} \quad (1)$$

where $\rho(\mathbf{r})$ and $\mathbf{c}(\mathbf{r})$ are the position-dependent mass density and elastic stiffness tensor, respectively. A correction factor in the modulus of the substrate's elastic stiffness tensor c_{ijmn} is introduced to account for the increased strain originating from the lattice mismatch at the interface between different materials.²⁰ We model this in terms of a spring, whose effective elastic constant increases when the system is initially stretched due to lattice mismatch. This correction factor thus depends on the phononic crystal's filling fraction. It is formalized in terms of a higher Young's modulus for the substrate (approximately +22% for 1D-SPC, +19% for 2D-SPC), and translates to an increased effective elastic stiffness tensor. The material properties for both the sapphire substrate and nickel stripes are listed in Table 1.

The acoustic eigenvalue problem is analyzed via transient finite element analysis. The simulation unit cell is illustrated in Figure 2b. The entire nanostructured composite is reproduced from the single unit cell. As required by the Bloch theorem, the displacements \mathbf{u}_1 and \mathbf{u}_2 calculated on opposite sides of the cell (see Figure 2b) are related by $\mathbf{u}_1 = e^{iK_x n \lambda} \mathbf{u}_2$, where $K_{x,n} = k_x + 2\pi n/\lambda$ and $k_x \in (-\pi/\lambda, \pi/\lambda)$. The simulations are performed

Table 1. Material Properties for 1D and 2D Surface Phononic Crystals: Young's modulus E , Poisson's ratio σ , and mass density ρ ^{18,20–22}

	E (GPa)	σ	ρ (kg/m ³)
1D-SPC			
Ni stripes	219	0.31	8900
Al ₂ O ₃ substrate	487	0.25	3980
2D-SPC			
Al disks	70	0.33	2700
Si substrate	156	0.27	2330

with $k_x = 0$, corresponding to the harmonics at the center of the surface Brillouin zone, as dictated by the symmetry of the experimental geometry. The displacement is fixed to zero on the bottom boundary and the height of the simulation cell is set to 100 μm, 2 orders of magnitude greater than the system's periodicity, a required condition to achieve an adequate density of states for the SPC.⁶ A refined quadratic-ordered mesh is chosen for accurate displacement calculations, considering the size discrepancy between the nanostructure and the substrate.

The calculated $\mathbf{u}(\mathbf{r}, t)$ is pictured in Figure 3 for increasing time delays. The time-sequence shows a displacement field confined within a depth λ from the top sapphire surface, which propagates to the bottom of the sapphire cell as time passes, as highlighted by the wave front in Figure 3b. The surface confined portion of the displacement field is therefore slowly dimmed during the evolution. The TRD experiment is sensitive to the displacement field at the surface of the SPC (see Figure 3a). The displacement field amplitude at the surface is in the picometer range after 100 ps; nevertheless it remains well detectable in actual experiments, as will be shown further on. The damping of the $\Delta I_{1d}/I_{1d}$ signal

recorded in experiments is due to the depletion of the surface confined energy into the far field, as shown in Figure 3b. In scattering terms, the near field, surface-confined solution of a pure semi-infinite slab, is scattered into the far field by the presence of the periodic grating. An analogy can be drawn with the scattering of surface plasmons into the electromagnetic far field by means of a periodic surface grating.

Spectral Decomposition: Pseudo-SAW, Fano Resonances and Lifetimes. In order to identify the modes that are effectively launched by the sudden expansion of the nanostructures, and quantitatively evaluate the relaxation process determining the oscillations' lifetime, we first calculate the set of eigenmodes $\{\tilde{\mathbf{u}}_i(\mathbf{r})\}$ solutions of the acoustic eigenvalue problem in the SPC geometry under investigation

$$\nabla \cdot [\mathbf{c}(\mathbf{r}) : \nabla \tilde{\mathbf{u}}_i(\mathbf{r})] = -\rho(\mathbf{r})\omega_i^2 \tilde{\mathbf{u}}_i(\mathbf{r}) \quad (2)$$

Spectral analysis of the time-dependent solution requires eigenvectors normalization. This is achieved defining

$$\mathbf{u}_i \equiv A_i \tilde{\mathbf{u}}_i \quad (3)$$

where A_i is a normalization constant calculated from

$$\langle \mathbf{u}_i | \mathbf{u}_j \rangle = \delta_{ij} \quad (4)$$

The scalar product between two displacement fields is defined as

$$\langle \mathbf{u}_i | \mathbf{u}_j \rangle \equiv \frac{C}{M} \int_V \rho(\mathbf{r}) \mathbf{u}_i(\mathbf{r}) \cdot \mathbf{u}_j(\mathbf{r}) dV \quad (5)$$

where M is the total phononic crystal mass, C is a unity constant of dimensions $[\text{m}^{-2}]$, and V is the total phononic crystal volume. The above orthonormalization and scalar product definitions are formally correct in that the acoustic eigenvalue equation outlined in eq 2 belongs to the set of Sturm-Liouville eigenvalue problems. Alternatively, the orthogonalization relation can be derived on a physical basis starting from mechanical energy conservation.²³

The eigenvectors \mathbf{u}_i are calculated at the center of the Brillouin zone ($k_x = 0$) and are therefore periodic functions with the same periodicity λ as the unit cell. The scalar product between two eigenvectors reduces to

$$\langle \mathbf{u}_i | \mathbf{u}_j \rangle \equiv \frac{C}{M_c} \int_{V_c} \rho(\mathbf{r}) \mathbf{u}_i(\mathbf{r}) \cdot \mathbf{u}_j(\mathbf{r}) dV \quad (6)$$

with M_c and V_c being the mass and volume of the unit cell. One thus obtains the normalized eigenvectors

$$\mathbf{u}_i = A_i \tilde{\mathbf{u}}_i = \sqrt{\frac{M_c}{C \int_{V_c} \rho \tilde{\mathbf{u}}_i^2 dV}} \tilde{\mathbf{u}}_i \quad (7)$$

The initial displacement is then projected on the set of eigenvectors $\{\mathbf{u}_i\}$

$$|\mathbf{u}(t_0)\rangle = \sum_i \langle \mathbf{u}_i | \mathbf{u}(t_0) \rangle |\mathbf{u}_i\rangle \quad (8)$$

The absolute value of the dimensionless projection coefficient $c_i \equiv \langle \mathbf{u}_i | \mathbf{u}(t_0) \rangle$ outlines to what extent the phononic crystal's eigenmode \mathbf{u}_i contributes to the impulsively excited displacement $\mathbf{u}(t_0)$.

Two resonances stand out in the plot of $|c_i|$ versus eigenmode frequency ν_i shown in Figure 4a. $|c_i|$ is not reported for the calculated frequencies covering the spectral window between

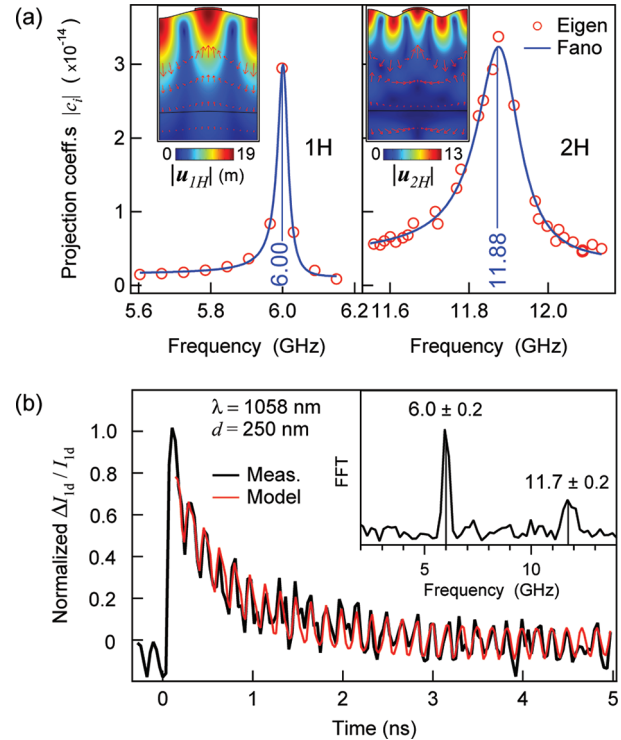


Figure 4. 1D surface phononic crystal. (a) Projection $|c_i|$ of the initial thermal expansion displacement on the symmetric eigenmodes of the composite system (red circles). The calculated curves are fitted with the function reported in eq 9 (blue line). Insets: absolute total displacement fields of the eigenvectors corresponding to the first (1H) and second (2H) harmonics pseudo-SAWs are reported within a depth of 1.2 μm. We point out that these displacement values need to be multiplied by $|c_i|$ in order to evaluate the pseudo-SAW contribution to $\mathbf{u}(t_0)$. (b) Normalized relative variation of the diffracted signal measured in the transient EUV diffraction experiment (black line). The pseudo-SAW frequencies from FFT of the signal are reported in the inset. The curve based on eq 16 is also reported (red line). The quantities ν_{1H} , ν_{2H} , τ_{1H} , τ_{2H} , q_{1H} , and q_{2H} are fixed to the values calculated theoretically in the projections, as reported in Table 2, whereas the coefficients B_1 , B_2 , and τ_{th} are left as free parameters (see text).

the two resonances, because the curve is featureless and with negligible values as compared to the resonances. The evaluation of the SAW-likeness coefficient $\alpha(\nu)$ for the resonating eigenmodes,⁶ together with the analysis of their displacement profiles (inset of Figure 4a), allow addressing them respectively as the first harmonic (1H), at $\nu_{1H} = 6.00$ GHz, and the second harmonic (2H), at $\nu_{2H} = 11.88$ GHz, cosine-like pseudo-SAWs.²⁴ The SAW-likeness coefficient evidences the different surface energy content of the calculated eigenmodes and identifies which modes have mechanical energy localized primarily within a depth λ .⁶ A remarkable feature in the plot of $|c_i|$ is the peculiar asymmetric line shape of the resonances, evoking Fano's profiles. A Fano profile is usually interpreted as the fingerprint of a configuration interaction (interference mixing) between a discrete and a continuum of states.²⁵ Within this picture, the present line shapes might well be the signature of the interference between the discrete phononic crystal's pseudosurface wave eigenmodes and the continuum of bulk modes. This evidence suggests fitting the resonances with the function

$$f(\nu) = K_0 + K_1 F(\nu) \quad (9)$$

Table 2. Frequency ν , Lifetime τ , and Fano Profile Index q of Pseudosurface Acoustic Wave Resonances Optically Excited in 1D-SPC^a

1D-SPC	ν (GHz)	τ (ns)	q
1H	6.00 ± 0.01	9.16 ± 0.33	-11.0 ± 2.5
2H	11.88 ± 0.01	2.44 ± 0.09	-11.5 ± 1.5

^aThe data are evaluated from the Fano line shape fit, based on eq 9, of the theoretically calculated pseudo-SAW resonances and displayed in the projection plot of Figure 4a (blue lines).

with the Fano function $F(\nu)$ being defined as

$$F(\nu) = \frac{2}{q^2 \Gamma_\nu} \frac{\left((\nu - \nu_0) + q \frac{\Gamma_\nu}{2} \right)^2}{(\nu - \nu_0)^2 + \left(\frac{\Gamma_\nu}{2} \right)^2} \quad (10)$$

The profile index q carries information on the configuration interaction, while Γ_ν is the line broadening parameter; ν_0 and K_0 are the fit horizontal and vertical offsets respectively, and K_1 is a dimensionless scaling factor. In order to clarify the meaning of the profile index, we recall that in the limit of $|q| \rightarrow \infty$, the above equation describes a symmetric Lorentzian line shape with broadening Γ_ν ,²⁶ whereas for $q = 0$ a symmetric antiresonance sets in. The pseudo-SAW frequencies ν_{1H} and ν_{2H} , line broadenings Γ_{1H} and Γ_{2H} , and asymmetry parameters q_{1H} and q_{2H} , as obtained from the fit for 1D-SPC, are listed in Table 2. The lifetimes τ_{1H} and τ_{2H} are calculated from $\tau = 1/\pi\Gamma_\nu$, as will become evident from eq 16. The shorter lifetime of the 2H pseudo-SAW correctly reflects its highly damped dynamics due to a tighter surface spatial confinement with respect to 1H pseudo-SAW, as shown in the insets of Figure 4a. The $|q|$ values are consistent with asymmetric line shapes dissimilar from a Lorentzian. On the basis of the quality of the fitting results, pictured as continuous lines in Figure 4a, a Fano line shape is thus ascribed to both the 1H and 2H pseudo-SAW resonances.

We now link the time-dependent traces $\Delta I_{1d}/I_{1d}$ expected in TRD experiments to the theory developed so far. The changes in $\Delta I_{1d}/I_{1d}$ are due to the modulation of the diffraction efficiency through modulation of the stripes' height h and width d . This modulation is caused by the excited modes having a strong surface displacement component. These modes are the ones identified by the resonances in the projection coefficient. In the literature, the experimental traces are usually rationalized within the following formula^{5,13,16}

$$\begin{aligned} \frac{\Delta I_{1d}}{I_{1d}}(t) = & y_0 + Ae^{-(t-t_0)/\tau_{th}} \\ & - B_1 e^{-(t-t_0)/\tau_{1H}} \cos(2\pi\nu_{1H}(t-t_0)) \\ & - B_2 e^{-(t-t_0)/\tau_{2H}} \cos(2\pi\nu_{2H}(t-t_0)) \end{aligned} \quad (11)$$

where the single exponential term accounts for the average stripes' height and width decay after expansion due to thermal flux from the stripes into the substrate. The damped oscillations mimic the pseudo-SAW modes surface displacement and account for energy dissipated into the bulk. Let us focus on the first damped oscillating term. We interpret it as arising from a

Lorentzian resonance in the angular frequency domain

$$\lim_{\gamma \rightarrow 0} \int_{-\infty}^{+\infty} L(\omega) e^{-\gamma\omega} e^{i\omega(t-t_0)} d\omega + c.c. \quad (12)$$

where

$$L(\omega) = \frac{\left(\frac{\Gamma_\omega}{2} \right)}{(\omega - \omega_{1H})^2 + \left(\frac{\Gamma_\omega}{2} \right)^2} \quad (13)$$

and $\tau_{1H} = 2/\Gamma_\omega$. Equation 12 represents a shifted Fourier transform in which the decaying exponential has been introduced to grant convergence of the integral when performed in the complex plane. We now substitute the Lorentzian line shape with a Fano into eq 12

$$F(\omega) = \frac{2}{q^2 \Gamma_\omega} \frac{\left((\omega - \omega_{1H}) + \left(\frac{q\Gamma_\omega}{2} \right) \right)^2}{(\omega - \omega_{1H})^2 + \left(\frac{\Gamma_\omega}{2} \right)^2} \quad (14)$$

thus obtaining in the time domain

$$e^{-(t-t_0)/\tau_{1H}} \left[\left(1 - \frac{1}{q_{1H}^2} \right) \cos(2\pi\nu_{1H}(t-t_0)) - \frac{2}{q} \sin(2\pi\nu_{1H}(t-t_0)) \right] \quad (15)$$

with $\tau_{1H} = 1/\pi\Gamma_\nu$. The time-dependent trace thus reads

$$\begin{aligned} \frac{\Delta I_{1d}}{I_{1d}}(t) = & y_0 + Ae^{-(t-t_0)/\tau_{th}} \\ & - B_1 e^{-(t-t_0)/\tau_{1H}} \left[\left(1 - \frac{1}{q_{1H}^2} \right) \cos(2\pi\nu_{1H}(t-t_0)) \right. \\ & \left. - \frac{2}{q_{1H}} \sin(2\pi\nu_{1H}(t-t_0)) \right] - B_2 e^{-(t-t_0)/\tau_{2H}} \left[\left(1 - \frac{1}{q_{2H}^2} \right) \right. \\ & \left. \times \cos(2\pi\nu_{2H}(t-t_0)) - \frac{2}{q_{2H}} \sin(2\pi\nu_{2H}(t-t_0)) \right] \end{aligned} \quad (16)$$

Equation 12 with $F(\omega)$ substituted for $L(\omega)$ is interpreted as the time evolution of a quasi-stationary state centered at ω_{1H} (ω_{2H}) and having line shape $|c_{1H}(\nu)|$ ($|c_{2H}(\nu)|$). The link between lifetime of a quasi-stationary state and its resonance width is automatically provided by the Fourier transform of the Fano line shape.

We stress that eq 11 is adopted in the literature as a fitting function arising from an heuristic classical oscillator model. The pseudo-SAW frequencies and lifetimes are extracted from the experimental data, with no a priori prediction being provided. Within the present model, eq 11 finds a formal justification in the case of a projection coefficient with symmetric line shape ($|q| \rightarrow \infty$). Equation 16 and its particular case eq 11 are based on a firm theoretical background relying on the concept of projection coefficients, and all the parameters entering the oscillating terms are calculated ab initio with exception for the B_1 and B_2 coefficients.

Benchmark on 1D-SPC. We benchmark our theoretical findings against time-resolved EUV diffraction experiments performed on an actual 1D-SPC displayed in Figure 2a. The SPC

was made by standard e-beam lithography and lift-off techniques. The parameters used in the experiments are the same as those adopted for the calculations on 1D-SPC.

The measured relative variation of the diffracted signal in the time-domain, $\Delta I_{1d}/I_{1d}(t)$, is displayed as a black line in Figure 4b. As expected, two dynamics are present in the experimental data: a damped oscillating component is superimposed on an exponential decay. The model (red line in Figure 4b) is compared with the experimental time-resolved trace fixing in eq 16 the oscillation frequencies, lifetimes, and asymmetry parameters to the calculated theoretical values reported in Table 2 and leaving as free fit parameters only the amplitudes B_1 , B_2 , and the coefficient τ_{th} . A frequency uncertainty of 0.2 GHz was allowed to account for the experimental frequency resolution (in the present case, the pump–probe time delay spans a window of 5 ns). The variable τ_{th} has been taken as a fitting parameter because of the uncertainty for the value of the Kapitza resistivity between the Ni stripes and the sapphire substrate. The fit outcome gives a $\tau_{th} = 656 \pm 42$ ps. An estimate based on an isothermal stripe in contact with a substrate, serving as a thermal reservoir at constant temperature, gives a Kapitza resistivity $\rho_{th} \sim 8 \times 10^{-9} \text{ m}^2 \text{ K/W}$. This value is compatible with thermal resistivity values expected for similar metal/dielectric interfaces.^{17,27} The good matching between the theoretical curve (red) and the experimental trace (black) in Figure 4b validates the developed theoretical framework and the correctness of the calculated values.

A few remarks can be made. First, despite the fact that the resonances in the projection coefficients are clearly asymmetric, an asymmetry value $|q| \gtrsim 10$ is practically similar to a Lorentzian when comparing the theoretical curve to the experimental time-resolved trace here reported. This is due to the way q enters eq 16. Nevertheless, the formula based on the Fano function gives drastically different results for $|q| \sim 5$ or less, this being the case for SPCs with higher pseudo-SAW/bulk modes coupling. Second, we note that two elastic resonances might have the same projection coefficient but contribute with different weights to the diffracted $\Delta I_{1d}/I_{1d}$ signal. For instance, in the 1D-SPC the fit parameter $B_1 \sim 2.5B_2$. This points to the fact that the first harmonic contribution to the diffracted signal is more important compared to the second harmonic, despite the higher elastic energy content in the 2H resonance (see Figure 4a). While interesting, linking the values of the projection coefficients involving the 1H and 2H pseudo-SAWs' elastic displacement profiles to the precise value of the relative diffracted electromagnetic intensity variation is not within the scope of the present paper.

Extension to 2D-SPC. The question arises whether the present findings are peculiar to the specific dimensionality and/or to the materials choice. To this end, the thermomechanical time-dependent model is extended to a 2D-SPC geometry consisting of an array of periodic aluminum nanodisks deposited on a silicon substrate. The nanodisks have diameter $d = 350$ nm, height $h = 45$ nm, and square array periodicity $\lambda = 1 \mu\text{m}$, thus giving a filling fraction $f \sim 0.1$, as seen in Figure 5a. The calculation is carried out assuming laser's parameters quite different from the previous case. Ultrafast near-infrared (NIR) laser probe pulses are employed in this TRD experiment instead of EUV. The apparatus is based on a Ti/sapphire oscillator with 120 fs pulse duration, 800 nm central wavelength, and $f_{rep} = 1$ MHz. The pump pulse energy is 1 nJ, and has a spot size $d_{pump} = 55 \mu\text{m}$ at fwhm.

The theory follows that outlined for the 1D case with the differences being in the simulation cell geometry and in the

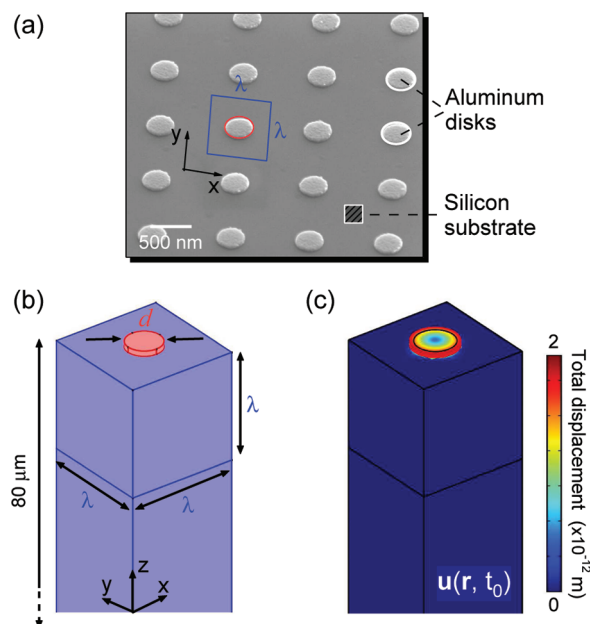


Figure 5. SEM image and simulation cell geometry of the 2D surface phononic crystal. (a) Elastic isotropic aluminum nanodisks of diameter $d = 350$ nm and height $h = 45$ nm are deposited on a crystalline silicon substrate. The grating has period $\lambda = 1 \mu\text{m}$. (b) The height of the simulation cell is $80 \mu\text{m}$ (only the top $2 \mu\text{m}$ portion is shown in the figure). (c) Total initial displacement profile of the expanded nanodisk calculated from the system's thermal profile at $t_0 = 2$ ps.

computational complexity involved. The simulation cell is reported in Figure 5b with Bloch periodic boundary conditions set on the sides to reproduce the entire phononic crystal. In the present case, the height of the silicon cell is reduced to $80 \mu\text{m}$, a value chosen to deal with the higher numerical complexity of finite element analysis in 3D, while matching the requirement on the density of eigenstates for the 2D-SPC simulation.⁶ The effective material properties for the Si substrate and Al disks are listed in Table 1. From the laser's parameters and the materials' thermal properties, we calculated that within $t_0 = 2$ ps the temperature of the metallic nanodisks is homogeneously increased by $\delta T \sim 4$ K with respect to the portion of the Si slab a few micrometers beneath the nanostructure/substrate interface. This value is ~ 15 times less than for 1D-SPC because of the lower pump pulse energy. Still, the temperature mismatch δT triggers a nonequilibrium expansion of the nanostructures, evaluated as $\delta x/x \sim 10^{-5}$ with x referring to both the nanodisk's diameter d and height h . The symmetric total displacement profile of the expanded nanodisk, $\mathbf{u}(\mathbf{r}, t_0)$ is reported in Figure 5(c).

The projection coefficients $|c_i|$ are obtained from eq 5, the eigenvalues \mathbf{u}_i being calculated for the present geometry. The fundamental pseudo-SAW at the frequency $\nu_{1H} = 5.23$ GHz and the signature of the 2H component at $\nu_{2H} = 10.43$ GHz are identified as the main contributions to the total displacement. Also for the 2D case the resonances have a clear Fano line shape (see Figure 6a). Making use of eq 9 to fit the theoretical 1H and 2H pseudo-SAW profiles, we also evaluate their lifetimes and asymmetry parameters. The results are listed in Table 3. Similarly to the 1D-SPC case, the wider Γ_ν broadening, and consequently short lifetime of the 2H component, are in agreement with the stronger surface confinement of higher harmonics and their greater mechanical damping due to elastic energy radiation to

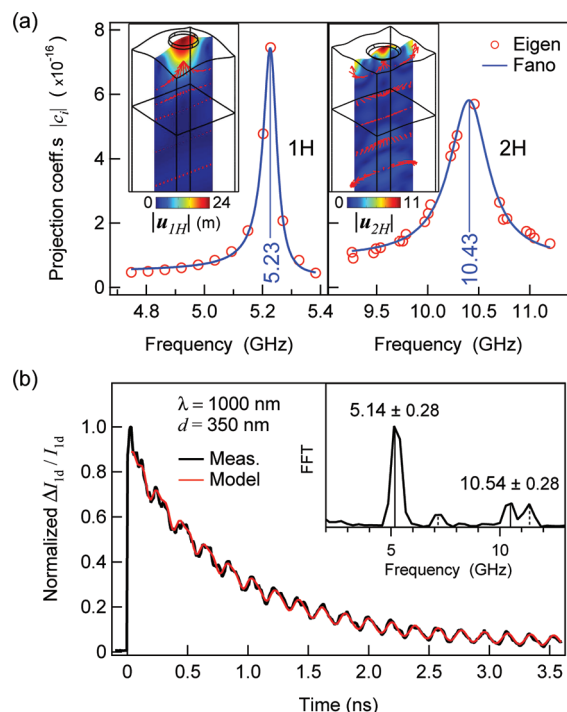


Figure 6. The 2D surface phononic crystal. (a) Projection $|c_i|$ of the initial thermal expansion displacement on the symmetric eigenmodes of the composite system (red circles). The calculated curves are fit by the function reported in eq 6 (blue line). Insets: absolute total displacement fields (slice) of the eigenvectors corresponding to the first (1H) and second (2H) harmonic pseudo-SAWs are reported within a depth of $2\ \mu\text{m}$. We point out that these displacement values need to be multiplied by $|c_i|$ in order to evaluate the pseudo-SAW contribution to $\mathbf{u}(t_0)$. (b) Normalized relative variation of the diffracted signal measured in the transient NIR diffraction experiment (black line). The pseudo-SAW frequencies from FFT of the signal are reported in the inset (solid lines). The curve based on eq 16 is also shown (red line).

bulk modes. Additional frequency components at 7.51 and 11.53 GHz (not reported in Figure 6a) enter the 2D projection as secondary (i.e., smaller amplitude) contributing terms to the impulsive expansion of the nanodisks. With a SAW-likeness coefficient⁶ on the order of 0.1 (higher than the usual ~ 0.01 featuring bulk modes, but far from the 0.6 value found here for pseudosurface modes) these additional components cannot compare with pseudosurface acoustic waves. Moreover, in the limit of filling fraction $f \rightarrow 0$ their bulklike displacement profile evolves to a pure bulk mode of the silicon slab. We thus classify them as bulk modes with a non-negligible surface component.

We benchmark our theoretical findings against time-resolved NIR diffraction experiments performed on the actual 2D-SPC displayed in Figure 5a. The SPC was made by standard e-beam lithography and lift-off techniques. The parameters used in the experiments are the same as those adopted for the calculations on 2D-SPC. The measured relative variation of the diffracted signal in the time-domain, $\Delta I_d/I_d(t)$, is shown in Figure 6b, together with the theoretical curve based on eq 16. In the FFT spectrum of the measured signal, two secondary peaks emerge as fingerprints of bulk modes with non-negligible surface component. The model (red line in Figure 6b) is compared with the experimental time-resolved trace fixing in eq 16 the oscillation frequencies, lifetimes, and asymmetry parameters to the calculated theoretical

Table 3. Frequency ν , Lifetime τ , and Fano Profile Index q of Pseudosurface Acoustic Wave Resonances Optically Excited in 2D-SPC^a

2D-SPC	ν (GHz)	τ (ns)	q
1H	5.23 ± 0.01	5.56 ± 0.18	-11.0 ± 1.5
2H	10.43 ± 0.02	0.67 ± 0.04	-25.5 ± 6.5

^a The data are evaluated from the Fano line shape fit, based on eq 9, of the theoretically calculated pseudo-SAW resonances and displayed in the projection plot of Figure 6a (blue lines).

values reported in Table 3, and leaving as free fit parameters only the amplitudes B_1 , B_2 , and the coefficient τ_{th} . Also in the present case, the fit outcome gives τ_{th} and ρ_{th} consistent with the values obtained for similar metal/silicon interfaces.²⁷ The matching between the theoretical curve and the experimental trace is excellent, confirming the validity of our model in describing the thermomechanics of SPC also in the 2D case.

The results give credence to this theoretical tool in demonstrating that pseudo-SAWs, as collective modes mainly confined on the surface of the SPC, are the main contribution to the dynamics following impulsive heating of periodic metallic nanostructures, and that the lifetime of these modes can be evaluated from first principles.

Spectral Analysis versus SAW-likeness. We now compare the information content carried by the SAW-likeness coefficient $\alpha(\nu)$ versus the projection $|c(\nu)|$. The resonances in $\alpha(\nu)$ identify which eigenmodes, if excited, are less subject to be scattered into bulk modes, but they give no information whatsoever on the acoustic eigenmodes that are actually excited in a time-resolved pump–probe experiment on SPCs. This information is provided by the resonances arising in $|c(\nu)|$. Furthermore, the resonance width Γ_ν allows quantitative access to the pseudo-SAW lifetime τ only in the case of $|c(\nu)|$. In fact, $\alpha(\nu)$ is evaluated on the basis of the solution to the eigenvalue problem described in eq 2, thus providing a static description. The projection $|c(\nu)|$ contains information on both the eigenvalue problem and the initial condition, thus providing a dynamic description.

To make this point clear let us consider a practical case. In the nice work by Sadhu et al.¹⁴ the modes excited in a time-resolved experiment on a SPC are calculated based on the resonances in $\alpha(\nu)$. Among the excited solutions in small filling fraction samples ($f \in [0.10; 0.25]$), the authors claim a sine-like eigenmode in the displacement profile. This odd symmetry solution, although being a pseudo-SAW, cannot be excited, and gives a null value for $|c(\nu)|$; the reason for this is that the initial radial displacement has even symmetry. Furthermore, if one is tempted to evaluate the pseudo-SAW lifetime from the fwhm of the resonance in the $\alpha(\nu)$ plot, instead of $|c(\nu)|$, in the case of the 1D-SPC investigated here he would get a 1H pseudo-SAW lifetime of 17.95 ± 0.07 ns and of 4.11 ± 0.47 ns for the 2H. These values contradict those measured experimentally. On the other hand the lifetimes calculated from the projection coefficient $|c(\nu)|$ match the experimental values very well.

The present model can be straightforwardly extended to predict the dynamics and lifetimes of impulsively excited pseudo-SAWs in SPCs other than at the center of the surface Brillouin zone. Such long-living pseudo-SAW modes have been recently demonstrated in SPCs exploiting a transient grating excitation scheme^{28,29} and foster great practical interest because of their extended lifetime.

Conclusions and Perspectives. In conclusion, we have performed an ab initio analysis of the dynamics following ultrafast optical excitation of hypersonic surface phononic crystals. A scheme is introduced to quantitatively access frequencies and lifetimes of the composite system's excited eigenmodes. By modeling the thermomechanics of 1D and 2D-SPCs from first principles, we calculated the initial heat-driven impulsive displacement of the structure. By spectrally decomposing the response, it is possible to identify eigenmodes Fano resonances that results from the coupling between surface and bulk acoustic modes. Most prominently pseudo-SAW excitation can clearly be identified, and their lifetimes calculated. The theory has been successfully tested against time-resolved optical diffraction measurements performed on both 1D and 2D surface phononic crystals over a wide range of material combinations and probing wavelengths.

The framework presented in this Letter is valuable in view of the application of photoacoustic techniques in nondestructive photoacoustic testing, metrology, and high-resolution acoustic imaging of embedded nanostructures. From a fundamental physics viewpoint, our findings expand the present knowledge on impulsive excitation and scattering of SAWs in mesoscale metamaterials, giving credence to our theoretical framework as a tool to understand the thermomechanics of hypersonic SPCs. Finally, the identification of Fano resonances in these composite systems highlights the physics shared in a large variety of systems,³⁰ including plasmonic metamaterials³¹ and photonic crystals.³²

AUTHOR INFORMATION

Corresponding Author

*E-mail: dnardi@dmf.unicatt.it.

ACKNOWLEDGMENT

We thank Dr. Pasqualantonio Pingue at NEST-SNS, Dr. Erik H. Anderson at CXRO-LBNL for valuable help on the fabrication of the devices, and Kathleen Hoozeboom-Pot at JILA-University of Colorado for valuable discussions. D.N., F.P., and F.B. acknowledge partial financial support by MIUR-PRIN 2008 project. The JILA group acknowledges support from the U.S. Department of Energy - Office of Basic Energy Sciences and the NSF Engineering Research Center for Extreme Ultraviolet Science and Technology.

REFERENCES

- (1) Hess, P. *Phys. Today* **2002**, 55, 42.
- (2) Rogers, J. A.; Maznev, A. A.; Banet, M. J.; Nelson, K. A. *Annu. Rev. Mater. Sci.* **2000**, 30, 117.
- (3) Antonelli, G. A.; Maris, H. J.; Malhotra, S. G.; Harper, J. M. E. *J. Appl. Phys.* **2002**, 91, 3261.
- (4) Tobey, R. I.; Gershgoren, E. H.; Siemens, M. E.; Murnane, M. M.; Kapteyn, H. C.; Feurer, T.; Nelson, K. A. *Appl. Phys. Lett.* **2004**, 85, 564.
- (5) Siemens, M. E.; Li, Q.; Murnane, M. M.; Kapteyn, H. C.; Yang, R.; Anderson, E. H.; Nelson, K. A. *Appl. Phys. Lett.* **2009**, 94, 093103.
- (6) Nardi, D.; Banfi, F.; Giannetti, C.; Revaz, B.; Ferrini, G.; Parmigiani, F. *Phys. Rev. B* **2009**, 80, 104119.
- (7) Antonelli, G. A.; Perrin, B.; Daly, B. C.; Cahill, D. G. *MRS Bull.* **2006**, 31, 607.
- (8) Maris, H. J. *Sci. Am.* **1998**, 278, 86.
- (9) Gronewold, T. M. A. *Anal. Chim. Acta* **2007**, 603, 119.
- (10) Lin, H.-N.; Maris, H. J.; Freund, L. B.; Lee, K. Y.; Luhn, H.; Kern, D. P. *J. Appl. Phys.* **1993**, 73, 37.
- (11) Hurley, D. H.; Telschow, K. L. *Phys. Rev. B* **2002**, 66, 153301.
- (12) Bonello, B.; Charles, C.; Ganot, F. *Appl. Phys. Lett.* **2007**, 90, 021909.
- (13) Giannetti, C.; Revaz, B.; Banfi, F.; Montagnese, M.; Ferrini, G.; Cilento, F.; Maccalli, S.; Vavassori, P.; Oliviero, G.; Bontempi, E.; et al. *Phys. Rev. B* **2007**, 76, 125413.
- (14) Sadhu, J.; Lee, J. H.; Sinha, S. *Appl. Phys. Lett.* **2010**, 97, 133106.
- (15) Banfi, F.; Pressacco, F.; Revaz, B.; Giannetti, C.; Nardi, D.; Ferrini, G.; Parmigiani, F. *Phys. Rev. B* **2010**, 81, 155426.
- (16) Giannetti, C.; Banfi, F.; Nardi, D.; Ferrini, G.; Parmigiani, F. *IEEE Photonics J.* **2009**, 1, 20.
- (17) Siemens, M. E.; Li, Q.; Yang, R.; Nelson, K. A.; Anderson, E. H.; Murnane, M. M.; Kapteyn, H. C. *Nat. Mater.* **2010**, 9, 26.
- (18) Weber, M. J. *Handbook of Optical Materials*; CRC Press: Boca Raton, FL, 2003.
- (19) Bozorth, R. M. *Ferromagnetism*; Wiley and Sons: Hoboken, NJ, 2003.
- (20) Zhu, R.; Pan, E.; Chung, P. W.; Cai, X.; Liew, K. M.; Buldum, A. *Semicond. Sci. Technol.* **2006**, 21, 906.
- (21) Auld, B. *Acoustic Fields and Waves in Solids*, Vol. II; Krieger Publ.: Malabar, FL, 1990.
- (22) Davies and Associates. *14ASM Metal Handbook*, 10th ed.; ASM International: Metals Park, OH, 1996.
- (23) Trallero-Giner, C.; Pérez-Alvarez, R.; García-Moliner, F. *Long Wave Polar Modes in Semiconductor Heterostructures*; Pergamon Press: New York, 1998.
- (24) The numerical simulation's accuracy and reliability, influencing the quality of the 2H projection and of projections for higher harmonics, are severely limited by the mesh refinement and consequently by the number of degrees of freedom handled, meaning ultimately by the calculation power of the workstation running the finite elements analysis software.
- (25) Fano, U. *Phys. Rev.* **1961**, 124, 1866.
- (26) Grosso, G.; Parravicini, G. P. *Solid State Physics*; Academic Press: San Diego, CA, 2000.
- (27) Swartz, E. T.; Pohl, R. O. *Appl. Phys. Lett.* **1987**, 51, 2200.
- (28) Maznev, A. A.; Wright, O. B. *J. Appl. Phys.* **2009**, 105, 123530.
- (29) Maznev, A. A.; Wright, O. B.; Matsuda, O. *New J. Phys.* **2011**, 13, 013037.
- (30) Miroshnichenko, A. E.; Flach, S.; Kivshar, Y. S. *Rev. Mod. Phys.* **2020**, 82, 2257.
- (31) Luk'yanchuk, B.; Zheludev, N. I.; Maier, S. A.; Halas, N. J.; Nordlander, P.; Giessen, H.; Chong, C. T. *Nat. Mater.* **2010**, 9, 707.
- (32) Galli, M.; Portalupi, S. L.; Belotti, M.; Andreani, L. C.; O'Faolain, L.; Krauss, T. F. *Appl. Phys. Lett.* **2009**, 94, 071101.